Sheet Resistance and Magnetoresistance in Polycrystalline CVD Graphenes

© *A.K. Fedotov*[1], *A.A. Kharchanka*[1], *U.E. Gumiennik*[1,2], *J.A. Fedotova*[1], *Ali Arash Ronassi*[3],
   A.S. Fedotov[4,5], *S.L. Prischepa*[6,7], *M.V. Chichkov*[8], *M.D. Malinkovich*[8]

[1] Institute for Nuclear Problems of Belarusian State University, Belarus
[2] AGH University of Science and Technology, Poland
[3] Payaame Noor University in Borujerd, Iran
[4] Belarusian State University, Belarus
[5] University of Tyumen, Russia
[6] Belarusian State University of Informatics and Radioelectronics, Belarus
[7] National Research Nuclear University MEPhI, Russia
[8] National University of Science and Technology MISiS, Russia

E-mail: akf1942@gmail.com

Temperature and magnetic field dependencies of sheet resistance $R_\square(T, B)$ in polycrystalline CVD graphene, investigated in the range of $2 \leq T \leq 300\,\text{K}$ and magnetic fields $0 \leq B \leq 8\,\text{T}$, allowed to determine carrier transport mechanisms in single-layered and twisted CVD graphene. It is shown that for $R_\square(T, B)$ curves for such samples are described by the interference quantum corrections to the Drude conductivity independently on type of precursor and peculiarities of graphene transfer from Cu foil onto the various substrates (glass or SiO_2). The twisted CVD graphene samples have demonstrated additional contribution of 2D hopping conductivity into the $R_\square(T, B)$ dependencies.

Keywords: graphene, single layer, twisted layers, CVD, carrier transport, magnetoresistance.

1. Introduction

In the last decade, graphene, one of the most important allotrope modifications of carbon nanomaterials, is widely studied due to its extraordinary physical properties. These initiate designing of various graphene-based hybrid structures for fabrication of their new types with additional functionalities which can be used in magneto- and gas sensitive sensors and transducers, spintronic devices, memristors, and other electronic devices, as well as for application in energy storage, thermoelectricity, magnetic bio-imaging, etc. [1–3]. However, using the exceptional properties of graphene for practical applications has proven to be a difficult task. The zero band gap, inherently low reactivity and solubility of pristine graphene preclude its use in several both high- and low-end applications [4].

It is known from literature that the unique properties of small samples of graphene (especially exfoliated) allowing the use of graphene in micro- and nanoelectronic devices are determined by many factors, like methods of graphene synthesis (micro-cleavage, chemical vapour deposition — CVD, plasma enhanced chemical vapour deposition — PECVD, epitaxy, etc.), the type of graphene (single-layered, multilayered, twisted, hybrid, vertical), dimensions of samples (with micron- or millimeter-sized width and length), as well as the type, concentration, and distribution of defects in graphene sheets [1–5]. It is obvious that

all these factors, in one way or another, should affect the mechanisms of carrier transport realized in graphene sheets. At the same time, studies of the effect of the substrate type, where graphene is transferred or deposited, on the conductivity of graphene give contradictory results. For example, in [6], it was reported that the electrical conductivity of graphene sheets is independent on the type of substrate used, while the authors of [7] demonstrated the dependence of electrical conductivity on the type of substrate. However, it is difficult to draw an unambiguous conclusion from these studies, which reason makes a greater contribution — methods of graphene synthesis, substrate itself, or the conditions for the transfer of graphene to it.

While considering mechanisms of carrier transport in graphene, one important feature of the available literature data should be noted, i.e., a vast majority of studies on electric conductivity, magneto-transport, Hall effect, and other electrical properties are devoted to micron-sized graphene layers obtained by micro-cleavage or cutting from polycrystalline samples (see, for example, citation lists given in well-known reviews [1–3]). However, as it was mentioned in [4], the micrometer-sized graphene sheets demonstrate, of course, outstanding electrical, mechanical, and chemical properties but they are too small for practical use in modern electronics, since the latter, for reasons of price/quality, requires large enough areas (no less than square centimeters).

Table 1. Graphene sheets types and characteristics

Number of sample	Manufacturer*	Number of layers in a sheet	Substrate	Growth method	Type of conductivity
1	RusGraphene (Russia)	One	Glass	CVD	p
2	RusGraphene (Russia)	One	SiO_2	CVD	p
3	MISIS (Russia)	One	SiO_2	CVD	n
4	BSUIR (Belarus)	Two, twisted	SiO_2	CVD	n

* Names of manufacturers are presented below.

Only in recent years, articles have appeared discussing the properties of graphene samples with sizes of several square millimeters and even centimeters, the best of which are usually obtained by CVD or epitaxy. In this sense, a series of articles published by an Israeli group from Bar-Ilan University [8,9], which have proved a strong heterogeneity of the commercial layers of CVD graphene, are indicative. In these articles, it is noted that on a graphene layer with an area of $5 \times 5 \, mm^2$ transferred onto a Si/SiO$_2$ substrate, it was possible to cut a very small number of samples $200 \times 200 \, \mu m^2$ in size, which had difference in values of the room-temperature sheet electrical resistivity no more than 10%. This strong inhomogeneity of properties by area was due to polycrystallinity of the initial CVD graphene sheet (the average grain size was about a few microns), as well as the influence of the procedure of graphene sheet transfer from copper foil onto substrate and the processes of electron-beam lithography at the preparation of electrical contacts.

Strong heterogeneity of the CVD layers of pristine polycrystalline graphene sheets means that in order to identify the integral characteristics of electrical transport (temperature and magnetic field dependences of electrical conductivity, Hall effect, mobility, etc.), it is desirable to carry out detailed measurements on samples with millimeter sizes and standard Hall geometry that are normally used in the most experiments in semiconductor physics.

Several mechanisms of electric carrier transport in magnetic field observed in graphene were discussed in literature. Most commonly, electrical conductivity in pristine graphene is described by the mechanism of electron wave function interference considered in the theory of quantum corrections to the Drude conductivity under the conditions of weak localization [10–16]. As reported in [16] for graphene produced by mechanical exfoliation, this mechanism includes several contributions to the breaking of electron wave function phase like low localization including electron–electron interaction [10,11,13–15], intervalley scattering and chirality [17], weak anti-localization [13,14], etc. The second important mechanism of electrical conductivity in strongly disordered graphene samples with large number of defects (including grain boundaries) is variable range hopping (VRH) of electrons over the localized states considered within the models of Mott [17–19] and Shklovskii–Efros [20] in zero external magnetic field and within the models of Mikoshiba [21] and Altshuler–Aronov–Khmelnitski [10] for conductivity in non-zero magnetic field.

To elucidate possible mechanisms of electric transport in polycrystalline pristine graphene, present paper is focused on the detailed investigation of variations in electrical conductivity and magnetoresistance in graphene large-area sheets grown in various labs and with different peculiarities of their transfer on dielectric substrates (glass and silica).

2. Experimental

A list of graphene sheets-on-substrate (G/S) used in our experiments along with their characteristics is presented in Table 1.

2.1. The technology of samples preparation

Samples 1−4 in Table 1 were obtained by CVD method on copper foils. Samples 1 and 2 were obtained in RusGraphene Company (Moscow, Russia) using a specially developed installation for the synthesis of graphene in a carbon-containing gas environment (CH$_4$) [22], in which a resistive method of current transfer was used to heat the catalytic substrate to temperatures above 800°C. For transferring from a copper foil to a dielectric substrate, the graphene film was coated with polymethyl methacrylate (PMMA) dissolved in anisole (concentration of 4 wt%). To dissolve the copper foil, the samples were immersed for 12 hours in a solution of ammonium persulfate $(NH_4)_2S_2O_8$ (concentration of 1 gram per 5 ml of water). The PMMA films with graphene were rinsed in deionized water and transferred onto a substrate, after which the polymer was removed by dissolving acetone for 20 minutes. The presence and quality of the graphene film on the surface of the cathode samples were confirmed by Raman spectroscopy.

It was shown in [22] that such kind of graphene sheets has a characteristic Raman spectra and can be identified as monolayer.

Type 3 samples were synthesized on a PlanarTech G2 facility MISiS (National University of Science and Technology, Moscow, Russia). Acetylene was used as a precursor; besides, for dilution, hydrogen was added to the reactor in the ratio $C_2H_2 : H_2 = 1 : 4$. The growth was performed at the temperature $1040°C$ at a pressure of 6 Torr. The transfer was performed using an intermediate substrate of PMMA film. A liquid polymer in the form of a 4% solution of PMMA in anisole was applied to a copper foil with graphene in a centrifuge at a speed of 1500 rpm, and was heated in an oven at a temperature of $150°C$. Copper was pickled in an aqueous solution of $FeCl_3$. The obtained PMMA film was rinsed twice in deionized water and laid on a substrate. After drying in a centrifuge at a speed of 3000 rpm, the film was heated at a temperature of $120°C$ to eliminate wrinkles. Removal of PMMA was carried out in acetone. After transfer to a dielectric substrate, type 3 samples of graphene possess a Raman spectrum characteristic of a monolayer (see [23]).

Type 4 samples were synthesized in BSUIR (Belarusian State University of Informatics and Radioelectronics, Minsk, Belarus) and were characterized with in-plane rotation of graphene layers by an angle $\theta \approx 11°$. They were fabricated by the method of atmospheric pressure chemical vapor deposition (AP CVD) on 25-μm thick Cu foil (Alfa Aesar 99.8% purity) from *n*-decane precursor $C_{10}H_{22}$ with nitrogen as a carrier gas, under experimental conditions previously reported elsewhere [24]. The transfer was performed after dissolution of Cu foil in 1 M of $FeCl_3$. After that, graphene sheets were rinsed out in distilled water and transferred onto SiO_2 dielectric substrate [25]. In [25,26], the twisted nature of the sample was established using Raman spectroscopy. Note that Hall measurements have shown *p*-type conductance in samples 1 and 2 and *n*-type conductance in samples 3 and 4.

2.2. Measurement methods

The temperature and magnetic field dependences of electrical resistance $R(T, B)$ were measured using four-probe method on a cryogen-free measuring system CFMS (Cryogenics Ltd, United Kingdom) based on a closed-cycle refrigerator in the temperature range $2 < T < 300$ K and in a transverse magnetic field with induction B up to 8 T. In the study of $R(T, B)$ dependences, the current through the sample was set and measured using a Keithley 6430 instrument, which made it possible to measure the electrical resistance of samples in the range from $100\,\mu\Omega$ to 20 GΩ with an accuracy of no worse than 0.1%. Relative magnetoresistance was defined as $MR = 100\%[R(B) - R(0)]/R(0)$, where $R(B)$ and $R(0)$ are resistances at non-zero and zero magnetic field inductions B, accordingly. Measurements were performed on the samples arranged on the contact pad (see Insets in Fig. 1), using 4
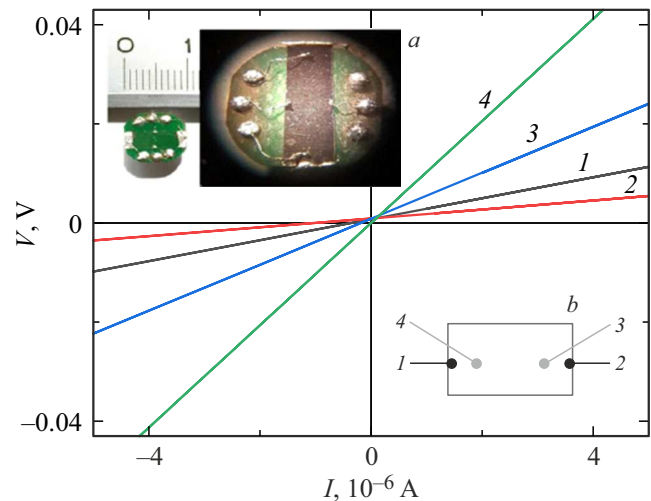

Figure 1. Current–voltage characteristics of the studied graphene samples at 300 K. The insets show photo of sample on contact pad (*a*) and scheme of electric probes arrangement (*b*) where *1, 2* are current contacts; *3, 4* are potential contacts. The numbering of the curves corresponds to the first column in Table 1.

indium (In) supersonically soldered electric contacts with soldered 50-μm diameter copper wires. Measurement cell with a sample on the contact pad was placed in a special measuring probe included LakeShore thermometers and magnetic field sensors, heaters, heated thermal shields, all in He gas atmosphere under low pressure. The probe was inserted into channel of superconducting solenoid inside the cryostat in CFMS. The temperature of the samples was controlled by LakeShore thermal diodes, calibrated with an accuracy of 0.0005 K and having a reproducibility of 0.001 K, which made it possible to stabilize and measure the temperature using the controller LakeShore 331.

In this study, $R(T)$ dependences were re-calculated into either sheet resistance

$$R_\square(T) = R(T)\frac{W}{L},\ \Omega, \tag{1a}$$

or into resistivity

$$\rho(T) = R(T)\frac{Wd}{L},\ \Omega \cdot m, \tag{1b}$$

or conductivity

$$\sigma(T) = \frac{1}{\rho(T)},\ Sm/m, \tag{1c}$$

where W and d are the width and thickness of the graphene layer, accordingly, and L is the distance between potential contacts 3 and 4 in Inset *b* at Fig. 1. Note that values of W and d were 4 and 11 mm accordingly, i.e., much more than were used in most experiments known from literature (usually, 10 to $200\,\mu$m). The error in $\rho(T)$ and $\sigma(T)$ measurements were mainly limited by the size of electric contacts and intercontact distances, and was equal or less than 5%. Installation details were previously described in [23,26].
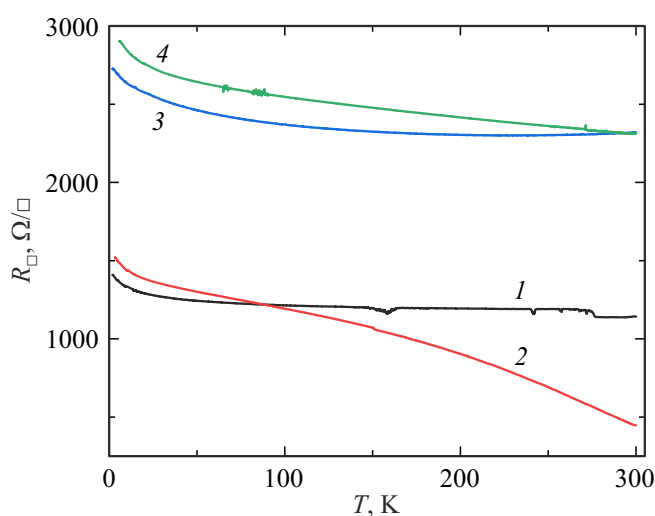
Figure 2. Temperature dependences of the longitudinal sheet resistance $R_\square(T)$ of the studied graphene samples. The numbering of the curves corresponds to the first column in Table 1.

3. Result and discussion

Before measuring the temperature and magnetic field dependences of the sheet resistance of the samples, we measured their longitudinal current–voltage $I(V)$ characteristics and Hall constant at room temperature ($T = 300\,\text{K}$). In all samples, the $I(V)$s turned out to be linear (Fig. 1), which indicates the ohmic behavior of the used electrical contacts.

The main features of the temperature dependences of the sheet resistance $R_\square(T)$ of different types of graphene samples from Table 1 are pictured in Fig. 2, independent on technological factors (growth features, a type of substrate, and conditions of sheet transfer).

Firstly, note that all the samples are characterized by the negative sign of the temperature coefficient of resistance (TCR) in almost the entire studied temperature range. Sample 3 is an exception because the sign of TCR becomes positive above 250 K. Secondly, the highest conductivity among all the studied samples was observed for single-layer samples 1 and 2 on glass and SiO_2 substrates, accordingly. Moreover, at temperatures below 85 K, the lowest resistance was in the sample 1 on glass, though at temperatures above 85 K the highest conductivity among all the studied samples was observed for the sample 2 on SiO_2 substrate. As is also seen from Fig. 2, the lowest conductivity in the entire studied temperature range was observed for the single-layer sample 3 and twisted sample 4 on SiO_2 substrates.

The influence of technological factors on the observed variations in $R_\square(T)$ dependences for the studied polycrystalline CVD graphene samples is analysed as follows.

Firstly, we should note strong difference in electric properties of graphene sheets grown by RusGraphene (samples 1 and 2) and that grown by MISIS and BSUIR (samples 3 and 4). This difference consists in less sheet resistance of samples 1 and 2 and their p-type conductance.

Samples 3 and 4 show n-type of conductance and higher sheet resistance (approximately 2 times). Since the type of precursors, growth temperature, and other parameters of CVD synthesis were practically the same, they could hardly have radically different influence on the type and value of the graphene layers sheet conductivity. However, there is yet one difference between these series of samples, which consists of the technique of transferring graphene layers from copper foil to substrates. This difference lay in the fact that during transfer of samples 1 and 2, copper was dissolved in ammonium persulfate, whereas for transfer of samples 3 and 4 iron chloride was used. It is known that ammonium persulfate is a stronger electron acceptor than iron chloride [22]. Since it is more difficult to rinse graphene from it before transfer, ammonium persulfate more strongly functionalizes graphene, which leads to an increase in the hole concentration and a decrease in the sheet resistance of samples 1 and 2 compared to samples 3 and 4.

Secondly, it turns out that the type of dielectric substrate, on which graphene sheets transferred from copper foil, is more unpredictable and undetermined influencing factor, which frequently results in contradictory behaviour of $R_\square(T)$ curves. For example, the comparison of curves *1* and *2* should reveal the effect of the substrate on the electrical properties of the samples, grown using similar technologies but obtained by transferring on different substrates (glass and silicon oxide, accordingly). However, the difference between these $R_\square(T)$ curves is noticeable only at temperatures above 100 K and is practically absent below 50 K. Moreover, for a sample on glass (curve *1*) fluctuations and jumps in resistance during measurement process can be seen. Such different behaviour of curves *1* and *2* does not allow to assign them only to the role of the substrate, i. e. without taking into account the effect of other influencing factors.

At the same time, a comparison of the $R_\square(T)$ curves for single-layer graphene samples 1 and 3 obtained by transfer to one type of substrates (silicon oxide) indicates their significant similarity, although, as mentioned above, these samples differ significantly in absolute values of sheet resistance due to difference in techniques of sheet transfer from copper foil on substrate. As presented in Fig. A1 of Appendix 1, in normalized coordinates $R_\square(T)/R_\square(250\,\text{K})$ the observed discrepancy between curves *1* and *3* does not exceed 3% below 100 K, and in the temperature range from 140 to 270 K this deviation does not exceed 0.2%. At the same time, sample 2, which has the same growth technology as sample 1 and the same substrate as sample 3, demonstrates at temperatures above 50 K the behavior of the $R_\square(T)/R_\square(250\,\text{K})$ curves different from samples 1 and 3 (Fig. A3). As was mentioned above, this is most likely due to the difference in transfer procedure, thereby indicating that in this case the effect of transfer is much more significant than that of the substrate type.

To identify possible mechanisms of carrier transport in the studied graphene samples, we re-plotted $R_\square(T)$ curves in various coordinate systems.
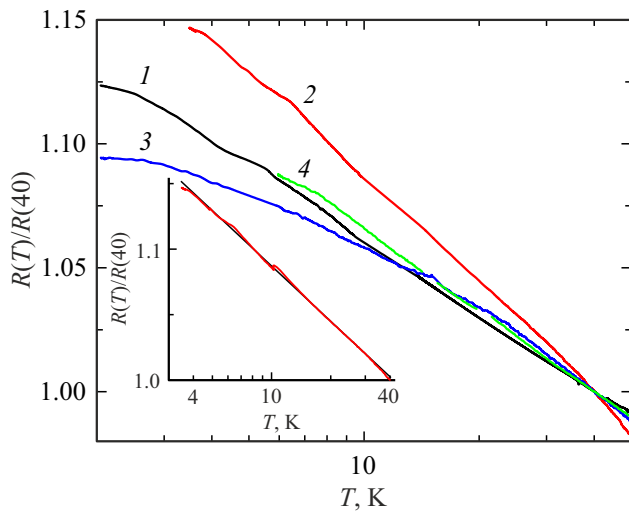
Figure 3. Low-temperature dependences of the normalized sheet resistance $R_\square(T)/R_\square(40\,\text{K})$ of the studied graphene samples on a semi-logarithmic scale. The numbering of the curves corresponds to the first column in Table 1. Inset: Example of linearized part of the $R_\square(T)/R_\square(40\,\text{K})$ curve for the sample 2 in a semi-logarithmic scale.

The analysis of the temperature dependences of the resistance in the Mott and Arrhenius scales [17,19,20] showed that, as in the case of sample 3 [23], samples 1 and 2 failed to reveal a noticeable contribution of hopping and/or tunneling mechanisms to their conductivity. At the same time, in the twisted sample 4, among other types of conductivity, the contribution from two-dimensional hopping transport was earlier revealed [26].

In order to reveal other possible low-temperature mechanisms of carrier transport, the $R_\square(T)$ dependences in Fig. 3 are shown on a semi-logarithmic scale and in normalized form $R_\square(T)/R_\square(40\,\text{K})$. The dependences re-plotted in the coordinates $R_\square - \text{Lg}T$ indicate the following two principal characteristic features of their behavior. First, in all samples in Fig. 3, independently on type of conductivity, we observed practically linear contributions at temperatures below 40 K. Such behavior is usually attributed to the mechanism of interference quantum corrections to the Drude conductivity [10,15,16,27] (mentioned in Introduction above) because of inelastic or quasi-elastic scattering of carriers by low-energy lattice vibrations and/or defects. The curves $R_\square(T)/R_\square(40\,\text{K})$ in Fig. 3 feature their saturation below
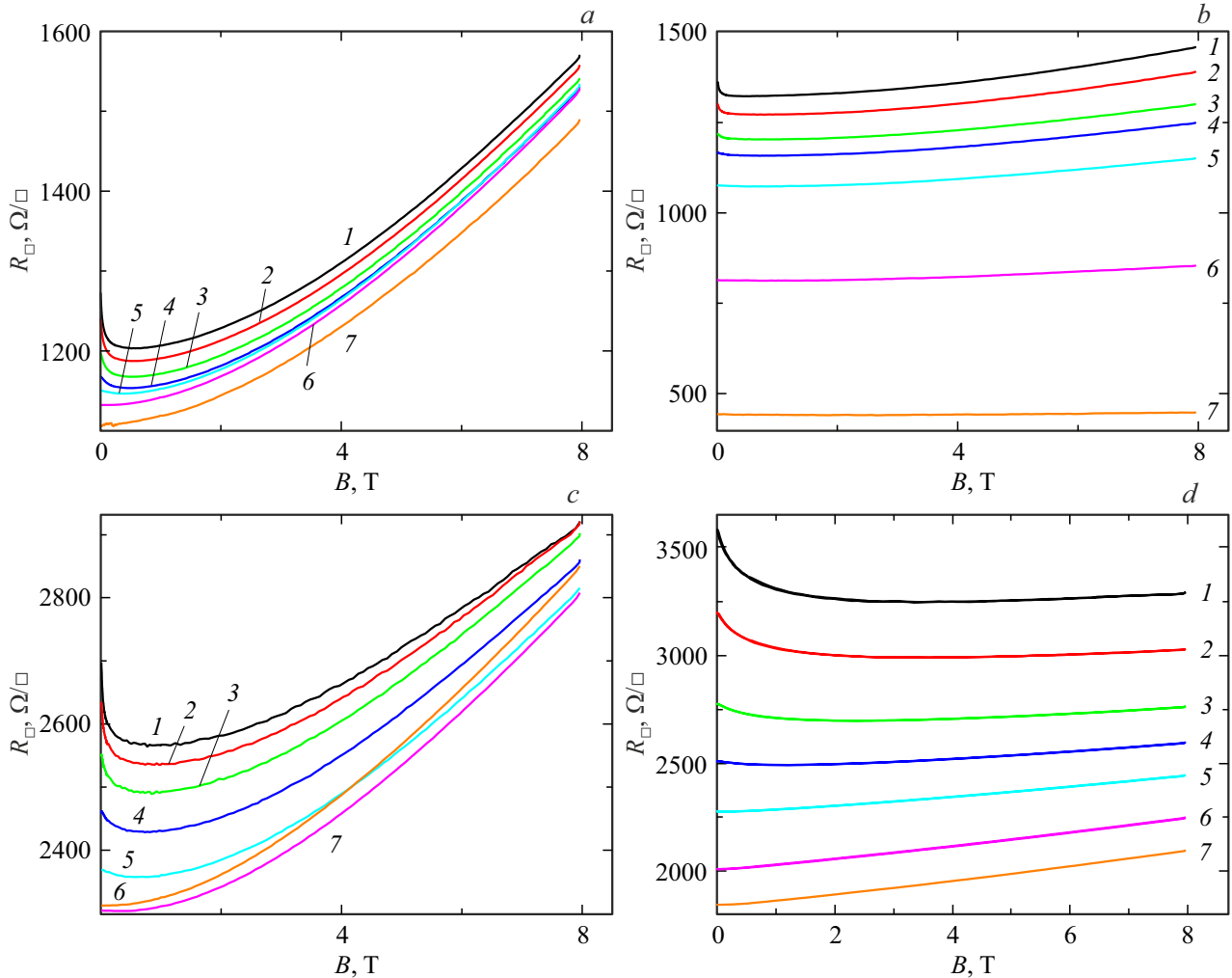

Figure 4. Dependences of sheet resistance on the induction of magnetic field B for the samples 1 (*a*), 2 (*b*), 3 (*c*) and 4 (*d*) at different temperatures T: *1* — 5, *2* — 10, *3* — 25, *4* — 50, *5* — 100, *6* — 200, *7* — 300 K.
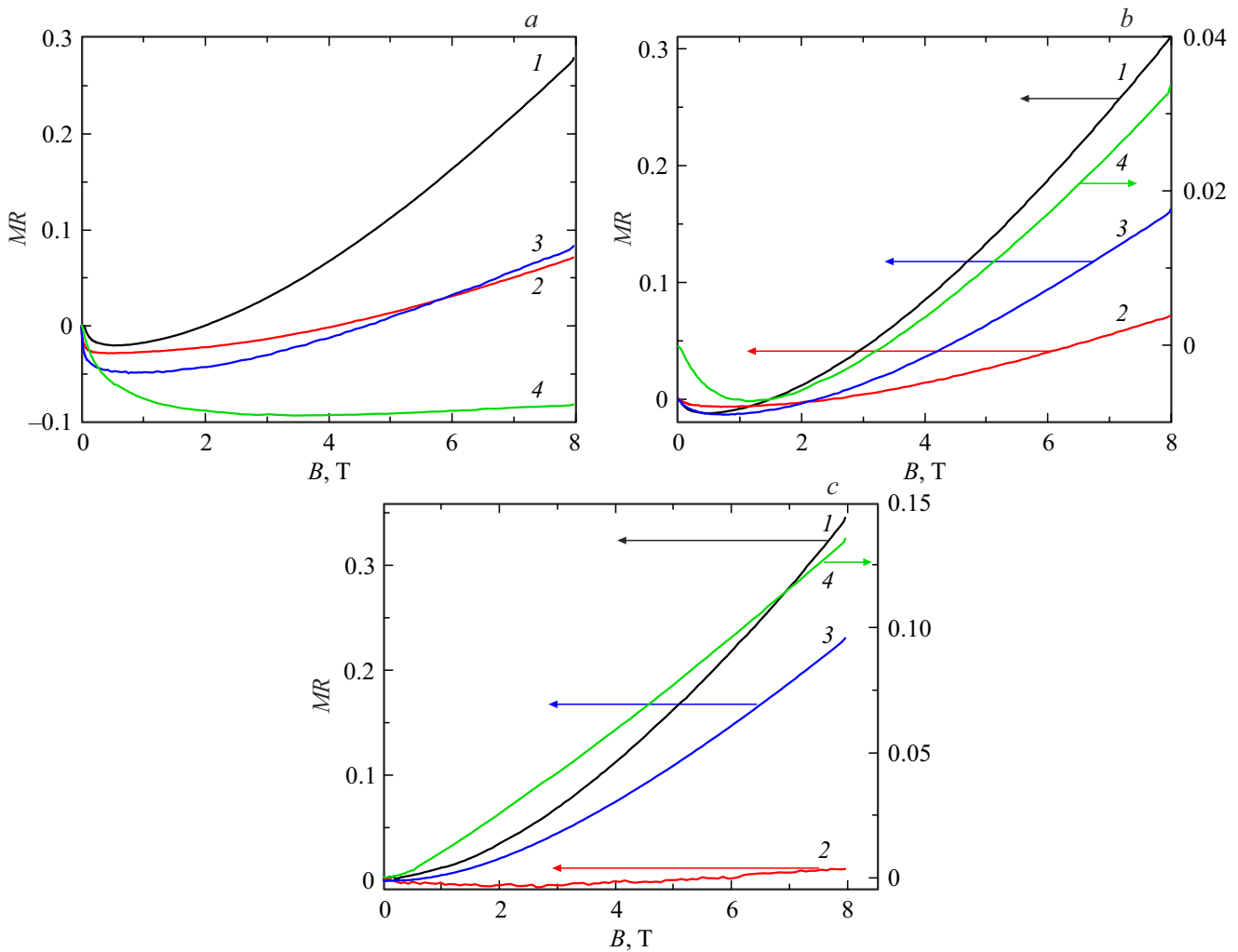
Figure 5. Dependences of the relative magnetoresistance $MR = [R_\square(B) - R_\square(0)]/R_\square(0)$ on the induction of the magnetic field B at temperatures $T = 5$ (a), 50 (b) and 300 K (c). The numbering of the curves corresponds to the first column in Table 1.

3−8 K, which may be due to a decrease in conductivity of graphene layers to its minimum value (to the so-called minimum metallic conductivity σ_{min}) as in disordered metallic systems when the temperature tends to absolute zero [12]. However, as we shall show below, there may be an alternative explanation for this saturation, which was done in [28].

To confirm the role of quantum corrections in $R_\square(T)$ dependences, the magneto-resistive effect was studied for all the samples. These results are presented in Fig. 4 as $R_\square(B)$ curves and in the form of the relative magnetoresistance $MR(B) = [R_\square(B) - R_\square(0)]/R_\square(0)$ in Fig. 5.

As can be seen from these figures, curves *1−4* are mainly characterized by two contributions to the magneto-resistive effect: negative (NMR) and positive (PMR). Their values depend on temperature and magnetic field. The proportion between NMR and PMR effects increases with the temperature decreasing. The NMR effect prevails in weak magnetic fields (below 0.4−0.8 T) and low temperatures (lower than 100 K), confirming the role of the above-

mentioned effects of weak localization in charge carrier transport in polycrystalline CVD graphene [9,16,29]. It is seen that PMR effect dominates in strong magnetic fields. In so doing, above 4−5 T, the dependences $R_\square(B)$ and $MR(B)$ for the studied samples are close to linear, whereas in weaker magnetic fields (but higher than 1 T) these curves look like squared, which indicates a possible effect of the Lorentz force on the charge carriers movement. Note that for these samples, the PMR effect gradually increases with temperature decreasing. At $B = 8$ T it approaches maximal values at $T = 2$ K being equal to 35, 22, and 13% for the samples 1, 3, and 4, respectively.

As can be seen, the NMR effect in the studied graphene samples exists at temperatures much higher than 10 K, which is unexpected for the two-dimensional gas in metallic and semiconducting low-dimensional films. In our opinion, this is possible due to high Debye temperature of graphene, which, according to [30,31], reaches 1000 K and even higher. This means that in graphene, corrections to the conductivity from weak localization can be caused by the

Table 2. Fitting parameters for the studied graphene samples

Sample number	Number of layers	Substrate	q	D, m^2/s	$\tau_\varphi \cdot 10^{-11}$, s	$\tau_i \cdot 10^{-13}$, s	$\tau^* \cdot 10^{-14}$, s
1	Single	Glass	0.89	0.006	1.11−0.14	6.51−2.76	2.56−4.37
2	Single	SiO$_2$	0.94	0.017	1.59−0.22	4.39−3.13	3.22−2.81
3	Single	SiO$_2$	0.99	0.015	1.36−0.18	3.37−2.05	1.31−1.91
4	Twisted	SiO$_2$	1.02	0.018	76.4−14.7	1.94−1.13	0.98−1.05

interaction of charge carriers with low-energy phonons. Inasmuch as their density is quite low at temperatures below 100 K, they do not lead to a phase breaking of the charge carriers wave functions observed in ordinary 2D semiconductors and metals with low values of Debye temperature.

Discuss in more detail the role of quantum corrections to the low-temperature Drude conductivity in the studied samples of polycrystalline graphene, based on the analysis of the magnetic field dependences of the sheet resistance described above. The main role of quantum corrections in the temperature range below 50 K is indicated by two main features of the $R_\square(T, B)$ and MR(T, B) curves in Figs 3−5: (i) the presence of linear sections on the curves [$R_\square(T)$ vs LgT] and (ii) the detection of NMR effect in magnetic fields lower than $(0.4-0.8)$ T, which is replaced by PMR effect with magnetic field and temperature increasing. These features of low-temperature magneto-resistive effect in the studied graphene samples indicate the possible co-existence of quantum corrections due to weak localization [28,32], but also due to other contributions leading to PMR effect even in the weak magnetic fields. According to [14,28,32,33], corrections related to intervalley scattering and violation of pseudo-spin chirality can also lead to PMR effect [28,32,33]. The listed combination of quantum corrections to the dependence of the graphene sheet resistance on the magnetic field $\Delta\sigma(B) = [\sigma(0) - \sigma(B)]$ are usually described by relations

$$\Delta R_\square(B) = -\frac{e^2\rho^2}{\pi h}\left[F\left(\frac{B}{B_\varphi}\right)\right.$$
$$\left. - F\left(\frac{B}{B_\varphi + 2B_i}\right) \pm 2F\left(\frac{B}{B_\varphi + B_*}\right)\right], \quad (2)$$

$$F(x) = \ln(x) + \psi(0.5 + x^{-1}), \quad (3)$$

where $\psi(x)$ is the digamma function. The parameter $x = B/B_{\varphi,i,*}$ in Eq. (2) is determined by the ratio of the induction of the external magnetic field B to the value of some characteristic field $B_{\varphi,i,*}$. According to relations

$$\tau_{\varphi,i,*} = \frac{\hbar c}{4eD}B_{\varphi,i,*}^{-1}, \quad (4)$$

where D is the electron diffusion coefficient, $\hbar$ is the reduced Planck constant, e is the electron charge, and c is the speed of light. The characteristic fields $B_{\varphi,i,*}$ in (4) determine the phase breaking times $\tau_{\varphi,i,*}$ of charge

carriers for the corresponding processes of inelastic or quasi-elastic scattering. The first term in Eq. (2) with the index φ corresponds to scattering under conditions of weak localization and determines the decoherence time τ_φ. The parameter B_i in the second term corresponds to the intervalley scattering time τ_i. The parameter B^* in the third term of Eq. (2) is due to the violation of chirality and the presence of „ripple" is due to warping of the graphene layer caused by thermal fluctuations. In this case, the characteristic time consists of two contributions

$$\tau_*^{-1} = \tau_w^{-1} + \tau_i^{-1}, \quad (5)$$

where τ_w is the time between scattering events due to warping on the average free path.

To estimate the characteristic times of the processes leading to the appearance of quantum corrections to the Drude conductivity in relation (2), we need to calculate the diffusion coefficient D of charge carriers. Below, in Appendix 2, we present the algorithm for the estimation of D based on the experimental values of conductivity and the work of Tikhonenko et al. [28]. This algorithm is given by Equations (A2-2)−(A2-5) and results in expression

$$D = \frac{\sigma kT}{e^2}\int_0^\infty f(E,\mu)\left[1 - f(E,\mu)\right]g(E)dE \quad (6)$$

for the effective diffusion coefficient which becomes possible to estimate the (effective) carrier diffusion coefficient. The estimated values of D for calculation of the characteristic times are presented in Table 2.

It follows from [12,28] that in the model of quantum corrections under conditions of weak localization, the temperature dependences of the phase breaking characteristic times τ_φ have a power-law form

$$\tau_\varphi(T) \sim T^{-q}, \quad (7)$$

where the exponent q is determined by the phase breaking mechanism, the theoretical values of which lie in the range $1 < q < 2$ [12].

Application of the fitting procedure to the experimental dependences $R_\square(T, B)$ for samples 1−4 based on Eqs (2)−(7) and (A2-1)−(A2-5) for weak magnetic fields $B < 1$ T gave the q, D, and $\tau_{\varphi,i,*}$ values presented in Table 2. The fitting results are shown in graphical form as well as in Fig. 6.
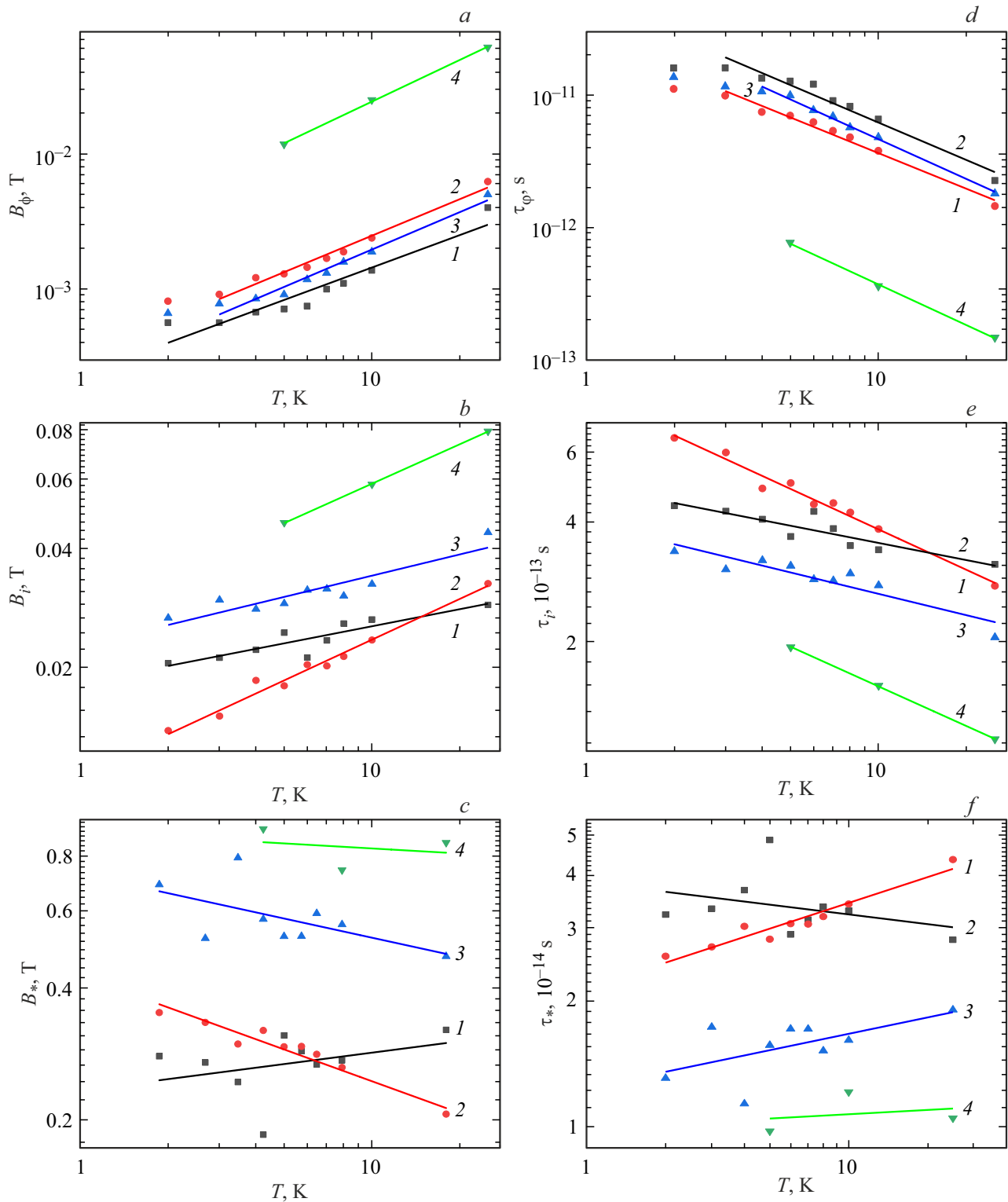
Figure 6. Temperature dependences of the characteristic magnetic fields $B_{\varphi,i,*}$ (a,b,c) and phase-breaking times $\tau_{\varphi,i,*}$ (g,e,f); for samples $1-4$ in Tables 1 and 2.

The fitting results confirm the power-law behavior of the temperature dependences of the phase breaking time τ_φ for the weak localization mechanism of type (7). As follows from the slopes of the lines in Fig. 6, the values of the exponent q are in the range of $0.90-1.04$ (see Table 2), which is close to 1. This indicates that the main contribution to the quantum corrections to the Drude conductivity can be attributed to inelastic carrier scattering by low-energy
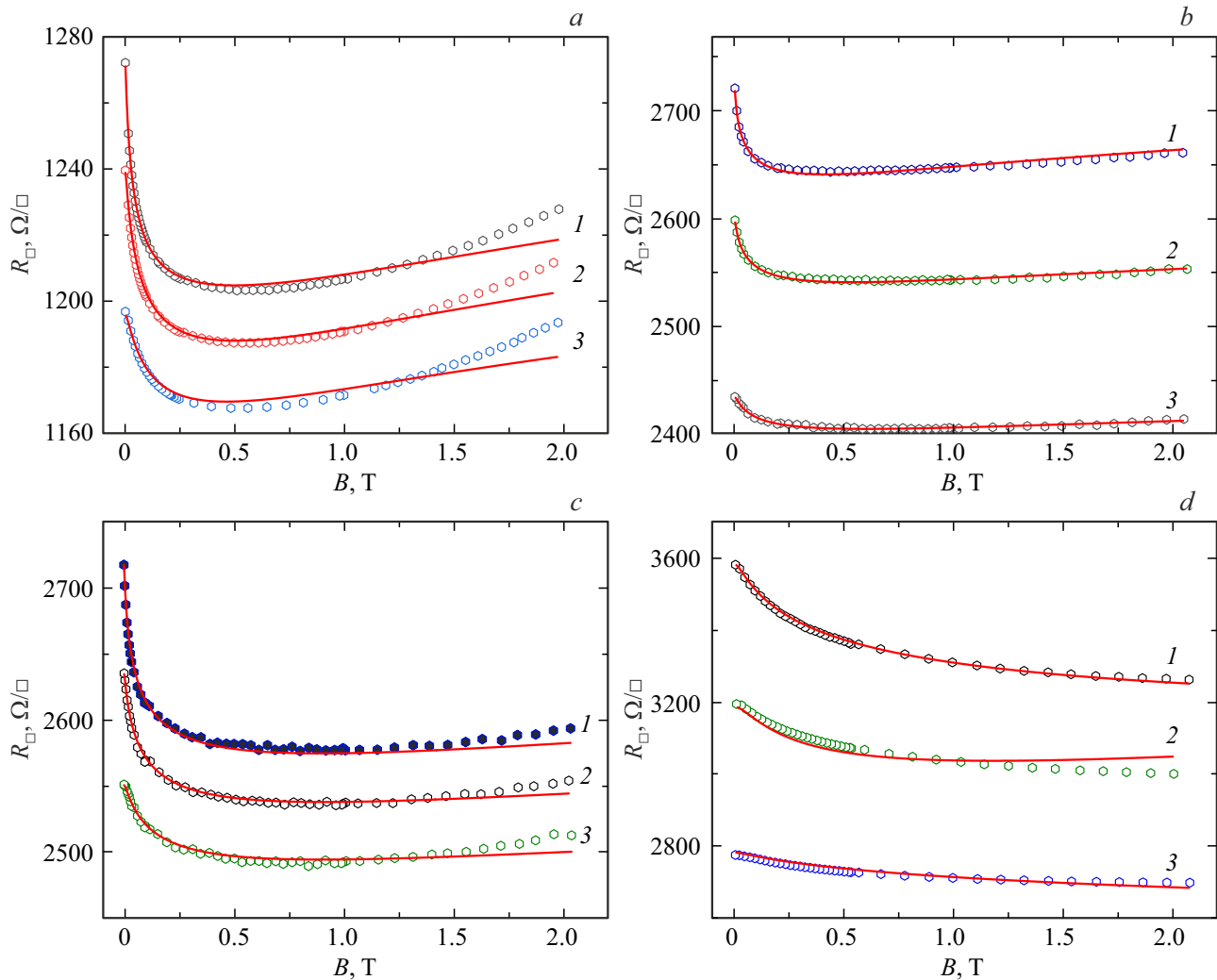
Figure 7. Dependences of the sheet resistance $R_\square(B)$ on the induction of magnetic field B for the samples 1 (*a*), 2 (*b*), 3 (*c*) and 4 (*d*) for the temperatures 5 (*1*), 10 (*2*) and 25 K (*3*). The solid curves indicate the fitted curves and the dots show experimental dependences.

phonons [12]. Moreover, τ_φ values for the single-layered samples 1−3 are practically independent on the type of substrate, sign of charge carriers, and the growth conditions. At the same time, the τ_φ values strongly decrease in the sample 4 of twisted graphene due to its higher disordering. As noted above, upon cooling of the samples, $R_\square(T)$ curves tend to saturation (Fig. 3), which was attributed in several studies to the minimum metallic conductivity σ_{min}. In the context of the analysis above, this behavior of the studied samples of polycrystalline graphene is more likely to be associated with the temperature dependence of the average free path of charge carriers, in particular due to its approaching the grain sizes when cooling [28].

As can be seen from a comparison of the characteristic times $\tau_{\varphi,i,*}$ and fields $B_{\varphi,i,*}$ included in relation (2) for the processes of inelastic and quasi-elastic scattering of charge carriers, they are almost the same for the contributions due to the violation of chirality and warping ($\tau^* \approx \tau_w$ and $B^* \approx B_w$), while the characteristic parameters of phase breaking for weak localization and intervalley scattering are significantly different, but always $\tau_i < \tau_\varphi$ and $B_\varphi > B_i$. Note also that, in the studied temperature and magnetic field ranges, the values of all parameters in Table 2, which are involved in the quantum correction model, are very similar to those given in the literature for other graphene types [34,35]. This indicates the adequacy of our description of the experimental $R_\square(B)$ curves by the quantum correction model, at least for the NMR effect region. In addition, note the closeness of the values of τ^* and τ_w, as well as their very weak temperature dependence (they show a small difference in these values in the range of 2−25 K, unlike that for τ_φ), according to [28], indicate independence of contributions due to violation of chirality and warping of deposits on the type of substrate.

Solid lines in Fig. 7 show the fitted $R_\square(B)$ curves, based on Eqs (2)−(7) at various temperatures, for the values of the characteristic magnetic fields $B_{\varphi,i,*}$ (or phase breaking times $\tau_{\varphi,i,*}$), presented in Table 2. As can be seen from

Fig. 7, *c* and *d*, the experimental and fitted curves $R_\square(B)$ in the temperature range $5-25$ K and magnetic fields $B \leq 2$ T practically coincide with each other for samples 3 and 4. In samples 1 and 2, the fitted curves begin to deviate significantly from experimental, starting from fields of approximately $1.3-1.5$ T. This indicates that the contribution from the PMR in the experimental dependences $R_\square(B)$ is described not only by the second and third terms of Eq. (2), but also, apparently, some other mechanisms that are not related to the model of quantum corrections (for example, because of the Lorentz-like or any other contributions).

Note that using only the weak localization contribution, i. e., only the first term of the Eq. (2), in the fitting procedure of the experimental dependences $R_\square(B)$ for the samples $1-4$, led to a discrepancy between the experimental and fitted curves beginning from $B \approx 0.4$ T. This indicates that the Eq. (2) gives more adequate description of the behavior of experimental $R_\square(B)$ curves (at least in the region of NMR effect and at the early stages of its transition to PMR) than if only the weak localization term in Eq. (2) is applied.

Summary

Comparative study of electric conductivity $R_\square(T)$ and magnetoresistance $R_\square(T, B)$ of CVD polycrystalline graphene deposited on different substrates and using different technological regimes clearly reveals that conductivity type (*n*- or *p*-type) measured by Hall effect is mainly governed by the technique of graphene transfer from Cu foil onto the selected substrate.

The observation of positive and negative contributions into magnetoresistance $R_\square(B)$ at $T < 40$ K and $B < 0.5$ T proves that electric conductivity of CVD single-layered graphene at T below 100 K is associated basically with interference quantum corrections to the Drude conductivity. Independently on fabrication regimes, in single-layered CVD graphene it originates from weak localization conditions due to the phase break of electron wave functions due to scattering on low-energy phonons and lattice defects, intervalley scattering, and violation of chirality, as well as layers warping. For the twisted CVD graphene, basing on the [17–21], we may conclude the additional contribution of 2D hopping conductivity into the $R_\square(T)$ and $R_\square(T, B)$ dependencies.

The developed approach allowed explaining experimental $R_\square(T, B)$ dependences for all studied samples with reasonable parameters of fit.

Acknowledgments

Funding

References

[1] A.C. Ferrari, F. Bonaccorso, V. Fal'ko, K.S. Novoselov, S. Roche, P. Bøggild, S. Borini, F.H.L. Koppens, V. Palermo, N. Pugno, J.A. Garrido, R. Sordan, A. Bianco, L. Ballerini, M. Prato, E. Lidorikis, J. Kivioja, C. Marinelli, T. Ryhänen, A. Morpurgo, J.N. Coleman, V. Nicolosi, L. Colombo, A. Fert, M. Garcia-Hernandez, A. Bachtold, G.F. Schneider, F. Guinea, C. Dekker, M. Barbone, C. Galiotis, A. Grigorenko, G. Konstantatos, A. Kis, M. Katsnelson, C.W.J. Beenakker, L. Vandersypen, A. Loiseau, V. Morandi, D. Neumaier, E. Treossi, V. Pellegrini, M. Polini, A. Tredicucci, G.M. Williams, B.H. Hong, J.H. Ahn, J.M. Kim, H. Zirath, B.J. van Wees, H. van der Zant, L. Occhipinti, A. Di Matteo, I.A. Kinloch, T. Seyller, E. Quesnel, X. Feng, K. Teo, N. Rupesinghe, P. Hakonen, S.R.T. Neil, Q. Tannock, T. Löfwander, J. Kinaret. Nanoscale **7**, *11*, 4598 (2015).

[2] Y. Liu, Z. Liu, W.S. Lew, Q.J. Wang. Nanoscale Res. Lett. **8**, *1*, 335 (2013).

[3] A.H.C. Neto, F. Guinea, N.M.R. Peres, K.S. Novoselov, A.K. Geim. Rev. Mod. Phys. **81**, *1*, 109 (2009).

[4] G. Ruhl, S. Wittmann, M. Koenig, D. Neumaier. Beilstein J. Nanotechnol **8**, *1*, 1056 (2017).

[5] Z. Yue, I. Levchenko, S. Kumar, D. Seo, X. Wang, S. Dou, K. Ostrikov. Nanoscale **5**, *19*, 9283 (2013).

[6] A.V. Butko, V.Y. Butko. Phys. Solid State **57**, *5*, 1048 (2015).

[7] S. Saha, O. Kahya, M. Jaiswal, A. Srivastava, A. Annadi, J. Balakrishnan, A. Pachoud, C.-T. Toh, B-H. Hong, J.-H. Ahn, T. Venkatesan, B. Özyilmaz. Sci. Rep. **4**, 6173 (2014).

[8] I. Shlimak, A. Haran, E. Zion, T. Havdala, Yu. Kaganovskii, A.V. Butenko, L. Wolfson, V. Richter, D. Naveh, A. Sharoni, E. Kogan, M. Kaveh. Phys. Rev. B **91**, *4*, 045414 (2015).

[9] E. Zion, A. Haran, A. Butenko, L. Wolfson, Y. Kaganovskii, T. Havdala, A. Sharoni, D. Naveh, V. Richter, M. Kaveh, E. Kogan, I. Shlimak. Graphene **4**, *3*, 45 (2015).

[10] B.L. Altshuler, A.G. Aronov, D.E. Khmelnitsky. J. Phys. C **15**, *36*, 7367 (1982).

[11] B.L. Altshuler, A.G. Aronov. Electron–electron interaction in disordered conductors. In: A.L. Efros, M. Pollak (Eds). Modern Problems in Condensed Matter Sciences. Elsevier (1985). https://doi.org/10.1016/B978-0-444-86916-6.50007-7

[12] V.M. Pudalov. Societá Italiana di Fisica **157**, 335 (2004). https://doi.org/10.3254/978-1-61499-013-0-335

[13] R.V. Gorbachev, F.V. Tikhonenko, A.S. Mayorov, D.W. Horsell, A. Savchenko. Phys. Rev. Lett. **98**, *17*, 176805 (2007).

[14] K. Kechedzhi, E. Mccann, V.I. Fal'ko, H. Suzuura, T. Ando, B.L. Altshuler. Eur. Phys. J. Spec. Top. **148**, *1*, 39 (2007).

[15] J. Jobst, D. Waldmann, I.V. Gornyi, A.D. Mirlin, H.B. Weber. Phys. Rev. Lett. **108**, *10*, 106601 (2012).

[16] S.V. Morozov, K.S. Novoselov, M.I. Katsnelson, F. Schedin, L.A. Ponomarenko, D. Jiang, A.K. Geim. Phys. Rev. Lett. **97**, *1*, 016801 (2006).

[17] B.I. Shklovskii, A.L. Efros. Electronic properties of doped semiconductors. Springer Series in Solid-State Sciences, Heidelberg (1984). 388 p.

[18] N.F. Mott. J. Theor. Experiment. Appl. Phys. **19**, *160*, 835 (1969).

[19] N.F. Mott, E.A. Davis. Electronic processes in non-crystalline materials, 2nd ed. University Press, Oxford (1979). 590 p.

[20] B.I. Shklovskii. Sov. Phys. Semicond. **6**, *12*, 1964 (1973).

[21] N. Mikoshiba. J. Phys. Chem. Solids **24**, *3*, 341 (1963).

[22] M.G. Rybin, V.R. Islamova, E.A. Obraztsova, E.D. Obraztsova. Appl. Phys. Lett. **112**, *3*, 033107 (2018).

[23] J.A. Fedotova, A.A. Kharchanka, A.K. Fedotov, M.V. Chichkov, M.D. Malinkovich, A.O. Konakov, S.A. Vorobyova, J.V. Kasiuk, U.E. Gumiennik, M. Kula, M. Mitura-Nowak, A.A. Maximenko, J. Przewoźnik, Cz. Kapusta. Phys. Solid State **62**, *2*, 368 (2020).

[24] I.V. Komissarov, N.G. Kovalchuk, V.A. Labunov, K.V. Girel, O.V. Korolik, M.S. Tivanov, A. Lazauskas, M. Andrulevičius, T. Tamulevičius, V. Grigaliūnas, Š. Meškinis, S. Tamulevičius, S.L. Prischepa. Beilstein J. Nanotechnol. **8**, *1*, 145 (2017).

[25] V.G. Bayev, J.A. Fedotova, J.V. Kasiuk, S.A. Vorobyova, A.A. Sohor, I.V. Komissarov, N.G. Kovalchuk, S.L. Prischepa, N.I. Kargin, M. Andrulevičius, J. Przewoznik, Cz. Kapusta, O.A. Ivashkevich, S.I. Tyutyunnikov, N.N. Kolobylina, P.V. Guryeva. Appl. Surf. Sci. **440**, 1252 (2018).

[26] A.K. Fedotov, S.L. Prischepa, J.A. Fedotova, V.G. Bayev, A.A. Ronassi, I.V. Komissarov, N.G. Kovalchuk, S.A. Vorobyova, O.A. Ivashkevich. Physica E **117**, *1−11*, 113790 (2020).

[27] K.J. Takehana, Y. Imanaka, E. Watanabe, H. Oosato, D. Tsuya, Y. Kim, K.-S. An. Current Appl. Phys. **17**, *4*, 474 (2017).

[28] F.V. Tikhonenko, D.W. Horsell, R.V. Gorbachev, A.K. Savchenko. Phys. Rev. Lett. **100**, *5*, 056802 (2008).

[29] A.M.R. Baker, J.A. Alexander-Webber, T. Altebaeumer, T.J.B.M. Janssen, A. Tzalenchuk, S. Lara-Avila, S. Kubatkin, R. Yakimova, C.-T. Lin, L.-J. Li, R.J. Nicholas. Phys. Rev. B **86**, *23*, 235441 (2012).

[30] V.K. Tewary, B. Yang. Phys. Rev. B **79**, *12*, 125416 (2009).

[31] Y. Xie, Z. Xu, S. Xu, Z. Cheng, N. Hashemi, C. Denga, X. Wang. Nanoscale **7**, *22*, 10101 (2015).

[32] K. Kechedzhi, V.I. Fal'ko, E. McCann, B.L. Altshuler. Phys. Rev. Lett. **98**, *17*, 176806 (2007).

[33] E. McCann, K. Kechedzhi, V.I. Fal'ko, H. Suzuura, T. Ando, B.L. Altshuler. Phys. Rev. Lett. **97**, *14*, 146805 (2006).

[34] E.N.D. Araujo, J.C. Brant, B.S. Archanjo, G. Medeiros-Ribeiro, E.S. Alves. Physica E **100**, 40 (2018).

[35] E.N.D. Araujo, J.C. Brant, B.S. Archanjo, G. Medeiros-Ribeiro, F. Plentz, E.S. Alves. Phys. Rev. B **91**, *24*, 245414 (2015).

Appendix 1

It is shown in the paper that the regimes of graphene samples fabrication evidently effect the type and value of their conductivity. For instance, samples 1 and 2 according to the Hall effect measurements are characterized by *p*-type of conductivity and quite close values of sheet resistance as compared to other considered CVD graphene samples. At the same time, shape of normalized $R_\square(T)/R_\square(250\,\text{K})$ curve for the sample 3 (graphene on SiO_2 substrate) is rather similar to that of the sample 1 (graphene on glass substrate) than for the sample 2 (graphene on SiO_2 substrate) (see Figs A1 and A2). It is seen that most pronounced deviation between curves for the samples 3 and 1 is generally no higher than 3% (Fig. A1), while in the temperature range between 140 and 270 K is even less comprising only 0.2%.

The peculiarity of samples 1 and 3 demonstrating two slopes on $R_\square(T)/R_\square(250\,\text{K})$ curves plotted in semi-logarithmic scale is worth noticing. It is seen from Fig. A3 that two linear sections are observed for these samples, namely in the temperature ranges $3−50$ and $50−120$ K for the samples 1; in the temperature ranges $5−20$ and $20−150$ K for the sample 3. This observation denotes possible similarity of physical mechanisms determining the shape of $R_\square(T)/R_\square(250\,\text{K})$ curves for samples 1 and 3.

At the same time, if one compares Figs A2 and A3, temperature dependencies of resistance for the sample 2 is very different from those for samples 1 (despite the similar technological regimes) and sample 3 (despite the same substrate used). Particularly, this difference becomes
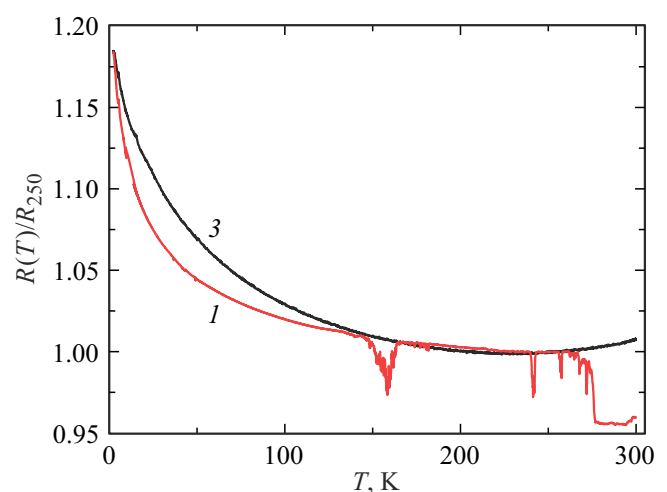

Figure A1. Temperature dependences of normalized sheet resistance $R_\square(T)/R_\square(250\,\text{K})$ in linear scale for samples 1 and 3 (curves *1* and *3*, respectively).
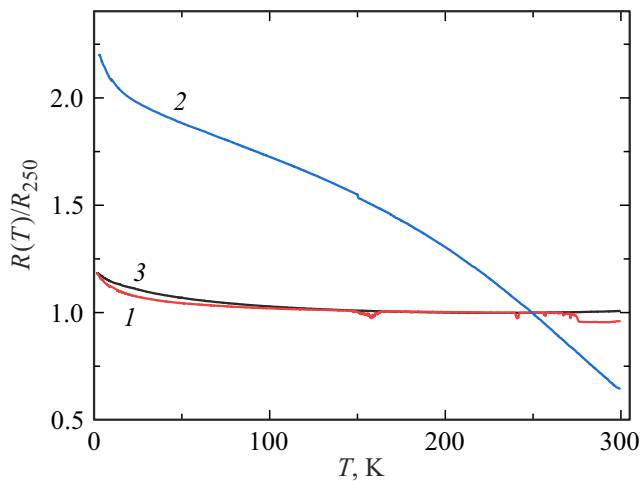
Figure A2. Temperature dependences of normalized sheet resistance $R_\square(T)/R_\square(250\,\mathrm{K})$ in linear scale for samples 1, 2, and 3 (curves *1, 2,* and *3*, respectively).
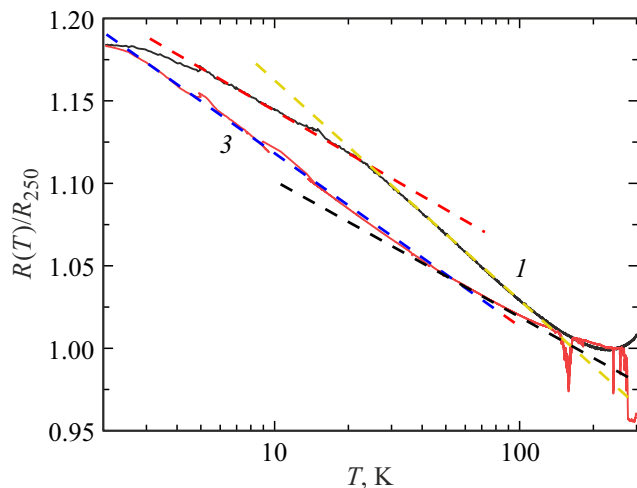

Figure A3. Temperature dependences of normalized sheet resistance $R_\square(T)/R_\square(250\,\mathrm{K})$ in semi-logarithmic scale for samples 1 and 3 (curves *1* and *3*, respectively).

apparent in stronger $R_\square(T)/R_\square(250\,\mathrm{K})$ dependency for the sample 2 as compared to the samples 1 and 3 (see Fig. A2), as well as in non-linear shape of this dependency when plotted in semi-logarithmic scale (see Fig. A3). The comparison of Figs 2 and 3 in the body text and Figs A1−A3 in this Appendix 1 allows to attribute such a distinction to some peculiarities of the transfer process of graphene on the substrate in these samples.

Appendix 2

In the work of Tikhonenko et al. jcite28 to evaluate the diffusion coefficient D in graphene, the following expression was proposed:

$$D = v_{\mathrm{F}} \frac{l}{2}, \qquad (A2\text{-}1)$$

where $v_{P\mathrm{F}}$ is the Fermi velocity of charge carriers, l is the average free path l equal to $\frac{h}{2e^2 k_{\mathrm{F}} n}$, k_{F} is the Fermi momentum and n is the concentration of charge carriers. Moreover, it is believed that only those charge carriers participate in conductivity that are on the Fermi surface. Thus, for defect-free graphene, this approach is most correct at low temperatures.

Since quantum corrections in the studied graphene layers are also observed at temperatures substantially higher than $25\,\mathrm{K}$ [10], we offer a more general approach for calculating D which can be used for high temperatures.

Let us represent the conducting sample as a homogeneous medium, neglecting the contribution of large-scale defects, for example, grain boundaries. We assume that the energy distribution of charge carriers is described by the Fermi–Dirac function $f(E) = \frac{1}{e^{\frac{E-\mu}{kT}}+1}$. Then the concentration of charge carriers can be described by the ratio

$$n = \int f(E)g(E)dE, \qquad (A2\text{-}2)$$

where $g(E)$ is the effective density of states in the band. We shall use the expression [34]

$$\sigma = e^2 D \left(\frac{\partial n}{\partial \mu}\right)_T, \qquad (A2\text{-}3)$$

for the relation between conductivity and diffusion coefficient. In this formula, the term $\left(\frac{\partial n}{\partial \mu}\right)_T$ characterizes the charge carriers involved in carrier transport under the impact of electric field. Since the chemical potential μ of carriers does not enter into the density of states $g(E)$, the relation (A2-4) can be rewritten in the form

$$
\begin{aligned}
\sigma &= e^2 D \int_{-\infty}^{+\infty} g(E) \frac{\partial}{\partial \mu}\left(\frac{1}{e^{\frac{(E-\mu)}{kT}}+1}\right) dE \\
&= \frac{e^2 D}{kT} \int_0^\infty g(E) \left(\frac{e^{\frac{(E-\mu)}{kT}}}{\left(e^{\frac{(E-\mu)}{kT}}+1\right)^2}\right) dE \\
&= \frac{e^2 D}{kT} \int_0^\infty g(E) f(E)(1-f(E)) dE. \qquad (A2\text{-}4)
\end{aligned}
$$

The relation for the diffusion coefficient just follows from the last expression

$$D = \frac{\sigma kT}{e^2} \int_0^\infty f(E,\mu)[1-f(E,\mu)]g(E)dE. \qquad (A2\text{-}5)$$

Using equations (A2-2)−(A2-5), it becomes possible to estimate the average (effective) carrier diffusion coefficient.

The proposed method for calculating the diffusion coefficient provides the following important advantages: (a) the ability to estimate D by changing the density of states $g(E)$ not only for single-layer graphene, but also for double-layer;

(b) the ability to take into account the energy distribution of charge carriers at temperatures significantly higher than for liquid helium boiling; (c) the possibility to take into account the shift of the Fermi level (chemical potential) μ when an external transversal electric field is applied to the sample (for example, when conductivity measuring with the third electrode).

The main limitation of this method application is that the relation (A2-5) between σ and D is correct only when we are dealing with diffusion (drift) conductivity. At low temperatures, the experimentally measured conductivity σ can also include the contribution from other mechanisms like hopping and others. Therefore, when assessing the diffusion coefficient D, it is necessary to make sure that a significant contribution of hopping conductivity is not observed in the most of the studied samples, or we can separate the hopping and drift-diffusion conductivity contributions, like in sample 4.